Submitted to

Sensors And Actuators B

Exploiting spectral information in Opto-Electronic Tweezers for cell classification and drug response evaluation

J. Filippi[1,2], D. Di Giuseppe[1,2], P. Casti[1,2], A. Mencattini [1,2], G. Antonelli[1,2], M. D'Orazio[1,2], F. Corsi[3], D. Della Morte Canosci[2], L. Ghibelli[3], C. Witte[4], C. Di Natale[1], S. L. Neale[4] and E. Martinelli [1,2]*

1. Department of Electronic Engineering, University of Rome Tor Vergata, Via del Politecnico 1, 00133 Rome, Italy
2. Interdisciplinary Center for Advanced Studies on Lab-on-Chip and Organ-on-Chip Applications (ICLOC), Via del Politecnico 1, 00133 Rome, Italy
3. Department of Biology, University of Rome Tor Vergata, Via della Ricerca Scientifica 1, 00133 Rome, Italy
4. James Watt School of Engineering, University of Glasgow, Glasgow, UK

Correspondence to:

Prof. Eugenio Martinelli

Department of Electronic Engineering

University of Rome Tor Vergata

Via del Politecnico 1, 00133 Roma, Italy

Email: martinelli@ing.uniroma2.it

Tel: +39 06 72597259

Abstract

Cell responses to varying electric fields can reveal insights on cell biology with important implications for pharmaceutical and basic research. In this work, we exploit spectral information content in Opto-Electronic Tweezers (OET) systems through machine learning for label-free characterization of cell dielectric properties aimed at cell classification and drug response evaluation. A customized Polymethyl-methacrylate (PMMA) chip with ITO substrates and an a-Si layer was designed for OET-based manipulation of cells and integrated with an inverted microscope. We obtained OET cell signatures as spectra responses of kinematic and dynamic descriptors, which are the result of time-lapse measurements at increasing frequencies of the OET. Machine learning algorithms enable automatic selection and characterization of the information content present in the OET signature so derived. Experiments are performed on three biological case studies, involving 1) the discrimination of cell types among U937 human leukaemia cells, PC-3 human prostate cancer cells and HaCaT human immortalized keratinocytes; 2) the evaluation of the effects of the chemotherapeutic agent etoposide on U937 cells at different concentrations; and 3) the evaluation of the effects of different exposure times of etoposide on U937 cells. The obtained results demonstrate that multiple levels of dielectric information can be extracted via OET cell signatures and clearly pose OET as a promising tool for cell discrimination and drug response evaluation.

Keywords: Machine Learning; multi-frequencies analysis; Opto-Electronic Tweezers; Lab-on-chip;

1. Introduction

Measurement of single-cell properties is extremely important in the fields of biology, medicine and chemistry, as it provides a means to understand the mechanisms of disease pathogenesis and to infer causal relationships between drug compounds and specific cell behaviours, supporting for instance cell-based therapies development and antibody discovery. The recent advances in micromachining and microfluidics are leading to an ever-increasing number of technologies, like impedance spectroscopy [1], magnetophoresis [2], dielectrophoresis (DEP) [3], and acoustophoresis [4], just to cite a few. Such systems, once integrated into microfluidic and lab-on-a-chip (LOC) devices, open up a plethora of possibilities for non-destructive and label-free analyses of cells. The utilization of optically defined electrodes in microfluidic systems, in particular, has gained special attention due to their ability to manipulate micro- and nanoscale particles in dynamic, contact-free, and flexible modalities [5]. With optoelectronic tweezers (OET), depending on the operational regime used under the influence of non-uniform electric fields [6], different types of optical manipulation techniques have been proposed over the last decades, including applications of light-actuated dielectrophoresis (DEP) [7–10], AC electro-osmosis (LACE) [11,12], and electrothermal flow [13].

Optically induced dielectrophoresis (ODEP) [7–10], also known as optoelectronic tweezers (OET), is emerging as a powerful technological solution for cell manipulation and characterization. OET combines the advantage of dielectrophoresis (DEP), in relating to the dielectric properties of the cells, with the flexibility of photosensitive surfaces in being responsive to dynamic optical patterns. In practice, OET "virtual" electrodes, realized by light projection, control the electric field landscape within the chip, allowing for DEP-induced sorting, separation, isolation, and manipulation of particles [14–17]. With respect to conventional DEP techniques, the virtual electrodes in OET enable flexible parallelization and automation of operations, thus improving the accuracy and efficacy of the measurements [18,19]. Moreover, if compared to optical tweezers (OT), in which the trapped force is generated by means of focused laser light, OETs require lower light intensity, facilitate parallel cell manipulation over a larger area, and are less expensive in terms of the fabrication process [5]. High throughput in ODEP is only limited by the field of view of the microscope used to visualize the cells but it can be increased by integration with a holographic imaging [20] or via multi-positioning facilities.

In the last decade, OET technology has been studied in a variety of life science scenarios. Cell-manipulation schemes have been optimized [21] and proved to be effective in separating living and dead cells [9,22], isolating circulating tumour cells [7,10,23], and sorting cells with different levels of drug resistance and viability [24]. The effectiveness of OET in such diversified experimental tasks reflects the key aspect that the dielectric properties of cells are closely related to their physiological status and thus indicative of many of their morphological, structural and chemical characteristics. As the effects of the electric field on the underlying mechanisms of polarization and conduction are specific to the biological material [25], there is space for researchers to investigate the physical properties of the cells by means of their responses to DEP forces. In recent works [19,26–28], the translation and rotation motions of cells in OET devices have been used to indirectly quantify the specific membrane capacitance of individual cells, cell conductivity and the values of crossover frequency. Acting as label free-biomarkers, such parameters have been related to different cell properties: the degree of malignancy [19], the responsiveness to drug concentration [26], the amount of cell deterioration [27], and cell apoptotic level [28].

ODEP represents a very powerful and promising technology for possible biomedical and multidisciplinary applications not yet addressed. With this in mind, in this work we tried to exploit new potentials of the OET devices in conjunction with microfluidic devices and machine learning. We present here extended functionalities of OET with the aim to provide a tool not only for cell manipulation but also for non-contact and in-depth single-cell characterization and investigations, gaining the simplicity in microfabrication and operation of ODEP.

First, cell types discrimination is performed with a new experimental set-up which allows reducing the power of the light incident on the cells without altering the dielectric properties of the culture medium and the shear and DEP forces exerted on the cells [29,30].

Second, exploiting that the dielectric properties of the cells vary across the frequency spectrum [31], we do not focus the analysis on a single cross-over frequency [19] but rather conduct a multi-spectral analysis by collecting the response of the system to a range of frequencies, assuming that each frequency content may carry individual and independent cell properties related to distinct phenomena (drug effects, cell-cell interaction, cell status, etc.) according to the specific applicative contexts.

In addition, we complement the information extraction with time-lapse microscopy for optical analysis of cell behavior and morphology, using automatic feature selection procedure and classification models, in order to conduct a variety of classification tasks, as demonstrated by way of example, by the three case studies presented in this work. We therefore propose here a platform that integrates an OET system, microfluidics, automatic cell-tracking, and machine learning, bridging the gap between the disposal of an experimental platform for single-cell manipulation and the characterization of cell dielectric properties. The frequency response spectrum, obtained by processing the video sequences of the DEP-induced cell motions, may represent a novel dielectric signature for the cell under measurement and represented the input of the next identification task of the cell subtyping.

With the aim of validating the proposed system and presenting possible important applicative scenarios, three different experiments have been considered. In the first experiment, we tested the ability of the system to discriminate among three different cell populations (human monocytic myeloid leukemia cell line U937, human prostatic carcinoma cell line PC3 and immortalized human keratinocytes HaCaT). The capacity to distinguish between the first two populations (i.e., human blood and epithelial tumor cells) represents a possible breakthrough in clinics, for instance, to help researchers typing and studying circulating tumor cells (CTCs) in human liquid biopsies. In the second experiment, instead, we tested the system in recognizing the effects of three different concentration levels of the chemotherapeutic agent etoposide on the dielectric alterations of U937, opening the window to a novel, original approach to classify tumor cell response to chemotherapy. A similar experiment aimed at investigating the impact of different drug exposure times was finally performed on PC3 cells, allowing to extend the results obtained in the second scenario to other tumor cells.

The strength of the proposed platform is therefore not limited to exploiting the new potential of an existent technology, but rather to demonstrate the general capability of the analysis in different biological tasks.

2. Materials and Methods

2.1 OET principle

OET devices are commonly made up of two plates of indium tin oxide (ITO)-coated glass separated with a spacer used to create the chamber containing medium liquid. The bottom plate is coated by a photoconductor, usually amorphous silicon (a-Si) or hydrogenated amorphous silicon (a-Si:H) of 1 μm thickness [9,18,23]. An AC potential at a certain frequency is applied between the top and bottom ITO layers. In the dark state, the impedance of the photoconductor is high and the electric field inside the chamber is uniform. When the photoconductor is illuminated by light, a non-uniform electric field is generated between the plates due to a decrease of the impedance of the photoconductor in the illuminated area so that “virtual electrodes” are created by the light pattern. The interaction between the non-uniform electric field and the polarizable particles produces a dielectrophoretic (DEP) force. For a homogenous spherical particle, the time-average of DEP force is defined as follows [31]:

$$\langle F_{DEP} \rangle = 2\pi r^3 \varepsilon_r \varepsilon_0 Re[K(\omega)] \nabla |E_{rms}|^2, \quad (1)$$

where r is the radius of the particle, $\varepsilon_r\varepsilon_0$ is the absolute permittivity of the surrounding medium, $E_{rms}$is the root-mean-square electric field, ω is the angular frequency, and $Re[K(\omega)]$ is the real part of the Clausius-Mossotti factor, with $K(\omega)$ is defined as follows:

$$K(\omega) = \frac{\varepsilon_p^* - \varepsilon_m^*}{\varepsilon_p^* + 2\varepsilon_m^*}; \qquad \varepsilon_p^* = \varepsilon_r\varepsilon_0 - j\frac{\sigma_p}{\omega}; \qquad \varepsilon_m^* = \varepsilon_r\varepsilon_0 - j\frac{\sigma_m}{\omega}. \tag{2}$$

In this case, ε_p^* and ε_m^* are the complex permittivity of the particle and the medium, respectively, and σ_p and σ_m are, respectively, the conductivity of the particle and the medium. A particle subjected to a DEP force can exhibit different kind of motion depending on the real part of the Clausius-Mossotti factor. In particular, if $Re[K(\omega)] > 0$, a positive dielectrophoretic force (pDEP) is exerted on the particle that moves toward the illuminated area. On the contrary, if $Re[K(\omega)] < 0$, a negative dielectrophoretic force (nDEP) is exerted on the particle and it moves away from the illuminated area. It should be noted that when $Re[K(\omega)] = 0$, the cell movement shifts from repulsive to attractive or vice versa and the corresponding frequency is called crossover frequency [26]. Whilst Equation 1 and 2 hold for homogeneous and spherical particles, cells being non-homogenous, a single-shell dielectric model can be considered, in which the cell is modelled with an external shell, represented by the cell membrane, and an internal region, which can be approximated as a relatively conductive homogeneous medium [26,29]. Therefore, the permittivity ε_p^* of cell becomes as follows:

$$\varepsilon_p^* = C_{mem}^* \frac{3r\varepsilon_{int}^*}{3\varepsilon_{int}^* + 3rC_{mem}^*}, \tag{3}$$

where r is the radius of the internal region, ε_{int}^* is the complex internal permittivity, and $C_{mem}^*$is the complex specific membrane capacitance (membrane capacitance per unit area), which is defined as follows:

$$C_{mem}^* = \frac{\varepsilon_{mem}}{d} - \frac{j\sigma_{mem}}{d}, \tag{4}$$

where ε_{mem} is the membrane permittivity, σ_{mem} is the membrane conductivity and d is the membrane thickness.

Being σ_m the medium conductivity, for frequencies below 1 MHz, the crossover frequency, f_{co}, can be defined, based on the single-shell model for a cell, by correlating the cell's dielectric properties with its membrane properties, as follows [19,32–34]:

$$f_{co} = \frac{\sqrt{2}}{2\pi r C_{mem}}\sigma_m, \tag{5}$$

where *r* is the cell radius, C_{mem} is the specific membrane capacitance. In this study, knowing σ_m and experimentally determining f_{co}, C_{mem} can be derived by Equation (5).

2.2 OET system setup

The proposed OET system is schematized in Fig. 1 with five main blocks: the microscope, the LOC, the AC voltage generator (composed of a function generator, an amplifier and an oscilloscope), a digital projector, and a PC station with a control unit and a machine learning engine. The LOC device is represented in entire and in section views including an overview of the cell manipulation performed during the experiments.

. The system was designed to extend the vitality of the cells during the analysis, and to increase the observation time to about two hours, which is pivotal for single-cell multi-frequency measurements. The video acquisitions and subsequent analysis are performed in a totally label-free manner, avoiding the damages induced by the use of fluorescence microscopy. This is possible due to the combined use of inverted microscopy, with the insertion of a band-pass filter, and of a customized LOC device. For more details on the system setup and the control unit we refer to sections S1 and S2 of the Supplementary Material.

2.3 Chip design and fabrication

The OET-based device was designed in Autodesk Inventor® and fabricated with a laser cut machine (Trotec Laser Inc., Austria). The overall view of the chip is showed in Fig. 2(a). It consists of three main parts: the holder (Fig. 2(b)), the channel (Fig.2(c)) and the top (Fig. 2(d)).
The holder was realised with three layers of Polymethyl-methacrylate (PMMA). The first (TroGlass Clear, Trotec Laser Inc., Austria) and the second layers (TroLase, Trotec Laser Inc., Austria) have thickness of 3 mm and 0.8 mm, respectively, and were assembled together with a laminated adhesive (467 M P transfer tape 3M™ Maplewood, US) and by pressing at 100 bar. The latter holds a copper strip tape (AT526, Advance Tapes International, Leicester, UK), used as electric connection for ITO substrate. The third PMMA layer has a thickness of 3 mm and was used as an adapter for the microscope stage and assembled with the previously described layers through screws.
The channel part is formed by two slides which are split via an adhesive layer and staggered to create the electrical contacts. The top slide (H: 1 mm, D: 25 mm, L:75 mm) is a glass coated with 200 nm thick ITO with two holes drilled using a drill (Dremel™, USA) at 3000 rpm. A portion of ITO was left uncovered to connect this slide to the copper contact located on the holder. The bottom slide (H: 1 mm, D: 25 mm, L: 75 mm) is a glass coated with 200 nm thick ITO upon which a 600 nm thick a-Si layer was deposited by plasma enhanced chemical vapour deposition (PECVD). A portion of ITO was left uncovered to connect a second contact, realized by laser cutting 3 mm of PMMA (TroGlass Clear, Trotec Laser Inc., Austria) and by covering it with a copper tape. The contact was placed on ITO and fixed with screws on the holder. The intermediate layer, that represents the proper channel, was obtained by laser cutting a double-sided adhesive tape. The two slides were cleaned with acetone and joined staggered together with the adhesive spacer by pressing gently and heating at 70 °C for 20 min. At the end of assembly, the height of chamber is about 60 μm.
The top part is created from two layers of PMMA to produce the reservoirs. In particular, the seventh layer (TroLase, Trotec Laser Inc., Austria) is 0.8 mm thick, the eighth layer (TroGlass Clear, Trotec Laser Inc., Austria) is 5 mm thick. The top part was assembled via adhesive tape and by pressing at 100 bar.
The three parts were assembled with screws. A picture of the device is shown in Fig. 2(e). An overview of the entire assembling process is available in Supplementary Video 1.

2.4 Cell culture

U937 human monocytic myeloid leukaemia cells, PC-3 human prostate cancer cells and HaCaT human immortalized keratinocytes were grown at 37°C in a 5% CO_2 humidified atmosphere. U937 and PC3 cells were cultured in RPMI 1640 medium supplemented with 10% fetal bovine serum, 2 mg/mL L-glutamine, 100 IU/mL penicillin and streptomycin (Euroclone). HaCaT cells were cultured in DMEM supplemented with 4.5 g/L glucose, 10% fetal bovine serum, 2 mg/mL L-glutamine, and 100 IU/mL penicillin and streptomycin (Euroclone). All experiments were performed on cells in the logarithmic phase of growth, under condition of > 98% viability (as determined by trypan blue exclusion). In each experiment, U937, PC3 or HaCaT cells were harvested, centrifuged, washed twice in phosphate buffered saline (PBS) and resuspended in the OET sucrose solution (8.5% sucrose, 1% PBS, 0.5% D-glucose) [9] at the final concentration of 0.1 x 10^6 cells/mL. PC3 and HaCaT, being adherent cells, were trypsinized (using Trypsin-EDTA) before centrifugation.

2.5 Determination of the operating conditions

The calibration process of the OET system setup was realized with polystyrene beads to assure repeatability of results and consistency with the literature [18]. Polystyrene beads of 20μm in diameter (Sigma-Aldrich, USA) were suspended in deionized water and 0.05% v/v of Tween 20. The buffer conductivity was measured as 5 mS/m. Suspensions with diverse conductivity values were obtained with an addition of a certain percentage of potassium chloride. For more details, please refer to Supplementary materials section S3. As a preliminary step of the measurement campaign, we looked into the optimal operating conditions for cell manipulation, including the choice of frequencies, the applied voltage, and the characteristics of the buffer solution. Given that the cell movement might be attractive or repulsive, depending on the medium conductivity, the cell type, the treatment, and the applied frequency/voltage [7,8,35], several tests were performed to understand the dielectric behaviours of different cell types inside the medium and, consequently, to determine the experimental parameters for the measurements. A conductivity of 15 mS/m was chosen for the buffer

solution to ensure a strong non-uniform electric field across the medium to facilitate cell manipulation. About 600 µL of suspended cells in buffer solution was pipetted inside the OET device. Both tanks were filled with the solution to avoid heating and evaporation.

2.6 Experimental protocol

The measurement consists of inducing a series of single-cell motions in response to a DEP force. The force is exerted by a rectangular light pattern (L: 54 µm, H: 288 µm), at varying frequencies of a fixed applied AC potential equal to 10 Vpp. Fig. 3 illustrates the experimental procedure for the measurement. Given an initial frequency value, f_{in} = 25 kHz, a frequency step, Δf = 5 kHz, increasing frequency values, $f = f_{in} + n \cdot \Delta f$, with n= 0,1,… n_{fin} and k_{fin} = 25, were applied for each new cell. Frequencies less than 25 kHz caused side effects including electrolysis that produced bubble formation, thereby cell membrane disruption and a-Si substrate damage [29]. Then, the n^{th} measurement is performed with the following steps: positioning on target, video recording, pattern projection, signal application, and characterization of the cell displacement. For each frequency, the measurement time for each cell is about 20-40 s (including 1-7 s for the OET-based experimental steps and additional 10-30 s for video processing and the extraction of the quantitative descriptors). The time needed over the complete frequency range is about 5 minutes. Each cell was analysed once to avoid possible damages induced by repeated measurements. The reproducibility of the procedure was assessed by performing multiple experimental replicas from independent cell cultures, which were obtained in different months.

2.6.1 Positioning on target

The cell under analysis is driven from its natural position to a specific target, which corresponds to the starting point of the measurement, by means of a projected light pattern (see Fig 3). The target point is fixed with respect to the projected pattern to ensure identical illumination conditions during the tests on different cells.
The initial positioning of the cell is performed as follows. The location of the cell inside the field of view of the microfluidic device's channel is automatically determined using a cell-detection software (whose details are reported in *Section 2.8.1*) and used to centre the projected light pattern on the cell's initial position. A pathfinding algorithm based on the potential field method [36,37] determines the best path going from the initial cell position to the target avoiding other cells, considered as obstacles. The running time of the algorithm is in the order of seconds and it has the potential to work in parallel for future applications. Attractive and repulsive potentials were set in correspondence of the target point and of the neighbouring cell positions, respectively. The obtained path is used as reference for leading the light pattern and carrying the cell at, a picked velocity, towards the target. For cells exhibiting a nDEP force at the initial conditions, i.e., 25 kHz and 10 Vpp, a doughnut-shaped pattern is used to drive the cell towards the target, as shown in Supplementary Video 2. On the contrary, for cells exhibiting a pDEP force, a circular light pattern is applied.

2.6.2 Video recording, pattern projection, and signal application

Once the cell is on the target, the measurement and video recording (20 frames/s) start with the application of the voltage at $f = f_{in}$. A rectangular light pattern, i.e., virtual electrode, is projected at a given distance from the target point (Fig. 3). This distance is kept constant for all the measurements in order to guarantee repeatable conditions of interaction between the generated electric field and the cell. Subsequently, the voltage is applied to generate the electric field. As a consequence, three motion scenarios are possible defining the displacement travelled from the start point to an end point (see Fig.3): 1) Cell motion under a nDEP force: the cell moves away from the projected pattern (repulsive motion); 2) Cell at the cross-over frequency: the DEP force vanishes, the cell remains steady (no cell motion); 3) Cell motion under a pDEP force: the cell moves towards the projected pattern (attractive motion). At the end of the cell motion, the recording is stopped, the function generator of the AC potential and the light are turned off. For the next frequency measurement if $k < k_{fin}$ the cell is repositioned on the target position, the frequency value is increased, and the procedure is repeated. Otherwise, the measurement ends.

2.7 Machine learning engine

2.7.1 Cell detection and tracking

For each video recording, cell tracking was performed using our custom software called *Cell Hunter*, already validated in our previous works [38–42]. It allows the detection of circular-shaped objects at every frame using the Circular Hough Transform (CHT) [43]. The centres of the localized cells in consecutive frames are linked together by using the Munkres algorithm [44] by solving an Optimal subpattern Assignment Problem (OAP). A smoothing spline approximation is derived from each track in order to reduce noise and unrealistic fluctuations of particles positions [45].

2.7.2 Features extraction

The f_{co} in Eq. (5) was experimentally determined in correspondence of the change of the sign of the DEP force, whilst the radius, r, for each cell was estimated with the CHT embedded in *Cell Hunter.* Given Eq. 5, the specific membrane capacitance C_{mem}, was derived.
At each frequency of analysis, two kinematic parameters and a dynamic parameter were extracted from the smoothed cell trajectories: the cumulative displacement, D_{f_n}, the maximum velocity, $v_{max}(f_n)$, and the maximum DEP force $F_{DEP\_max}(f_n)$, respectively. A total of three response spectra were determined for each cell. Feature extraction and subsequent data analysis have been performed in MATLAB® 2020a. Details on the computation of the response spectra are reported as follows.

Cumulative displacement

The displacement along the x-axis, D_{f_n}, was calculated at frequency, f_n, as:

$$D_{f_n} = x_{end}(f_n) - x_{start}(f_n), \tag{6}$$

where $x_{end}(f_n)$ and $x_{start}(f_n)$ are the x-axis coordinates of the centre of the cell, respectively, at the ending and at the starting point of the trajectory generated at frequency f_n. Measurements are repeated for frequency values, f_n, with $f_n = f_{in} + n\,\Delta f$, $f_{in} = 25$ kHz, $\Delta f = 5$ kHz, and n = [0,1,…,25]. For each considered frequency, f_n, we derived a cumulative displacement, $CD(f_n)$, by summing all the displacements, D_{f_i}, obtained up to the frequency f_n, as follows:

$$CD(f_n) = \sum_{i=1}^{n} D_{f_i} \tag{7}$$

Maximum velocity

For each trajectory generated at frequency f_n, we calculated the instant velocity *v*(t) along the track, by differentiating the coordinates of the cell (*x*(t), *y*(t)) with respect to time [39]. The maximum velocity values computed along the trajectory of the cell generated for all the frequencies f_n , i.e., $v_{max}(f_n)$ were then used as descriptors in the classification model.

Maximum DEP force

By knowing the maximum velocity and the cell radius, we calculated the maximum DEP force, at each frequency, as follows.
Based on the assumption that the OET fluid system operates in laminar flow regime (Reynold number: Re << 1), the DEP force acting on cells (see Equation 1 in Section *2.1 Principle*) can be considered equivalent to the drag force, given by Stoke's law [3,21,22]:

$$F_{drag} = 6\eta\pi r v, \tag{8}$$

where η is the dynamic viscosity of the fluid medium, r is the cell radius and v is the cell velocity [6,18,30]. As a general assumption, when a spherical particle translates near a surface, the Stoke's law is affected by an error, so the force must be scaled via the Faxen's correction [46,47].

It is important to note that in our OET device the distance between the top and the bottom plate is 60 μm, so a cell moves close to the two walls (grazing to bottom plate). Therefore, we considered the followed Faxen's correction K_f [24]:

$$K_{\mathcal{F}} = \frac{1}{1 - \left(\frac{9}{16}r\right)\left[\left(\frac{1}{l_1}\right) + \left(\frac{1}{l_2}\right)\right]} \tag{9}$$

where l_1 is the distance between the centre of cell and the top plate and l_2 is the distance between the centre of cell and the bottom plate. In our case, $l_1 = 60$ μm – r and $l_2 = r$. Hence, we obtain:

$$F_{DEP} = K_{\mathcal{F}} F_{drag}. \tag{10}$$

In particular, the maximum DEP force was computed as follows:

$$F_{drag\_max}(f_n) = 6\eta\pi r v_{max}(f_n). \tag{11}$$

$$F_{DEP\_max}(f_n) = K_{\mathcal{F}} F_{drag\_max}(f_n). \tag{12}$$

2.7.3 Data analysis

The three features described above, i.e., $CD(f_n)$, $v_{max}(f_n)$, and $F_{DEP\_max}(f_n)$, were calculated for frequency values over the range [25 - 150] kHz, and a response spectrum was obtained for every cell analysed. The range of frequencies [55-100] kHz, in which all cells for all the case studies survived, was considered for further analysis. Therefore, we have taken into account a total of 30 features (10 frequency values for each kind of feature). To reduce correlation among the features, we performed a sequential feature selection (SFS) [48] in two steps, so that only the most significant descriptors were extracted for each biological problem considered. Firstly, with a backward SFS procedure, a subset of features was selected. Then, on this set, a forward SFS was carried out to determine the final set of descriptors [49,50]. For each case study, and the corresponding set of features so derived, a LDA (Linear Discriminant Analysis) model was used for pattern classification and validated with a five group venetian-blinds cross-validation [51].

2.8 Biological scenarios

Three case studies were investigated. Briefly, in the first scenario we tested the ability of the system to discriminate among three different cell populations (human monocytic myeloid leukemia cell line U937, human prostatic carcinoma cell line PC3, and immortalized human keratinocytes HaCaT). In the second scenario, we explored the possibility to recognize the effects of three different concentration levels of the chemotherapeutic agent etoposide on U937, by measuring cell dielectric alterations through the alteration of the OET cell spectrum. In the last scenario, instead, we extended the results obtained in the second scenario to other tumor cells (i.e., PC3 cells), investigating the impact of different drug exposure times on the OET cell spectrum.

2.8.1 Case Study 1: discrimination of heterogeneous cell population

Case Study 1 investigates the capability of the OET-based measurement system of discriminating cell populations according to the cell type. Three cell populations were considered for a total number of 83 measured cells including replicas from different aliquots of cell suspensions: 22 U937 cells (3 replicas), 33 PC3 cells (3 replicas) and 28 HaCaT cells (2 replicas). Whilst U937 and PC3 cells exhibited both nDEP and pDEP, HaCaT cells exhibited only a pDEP force in the selected frequency range of [25-150] Hz.

2.8.2 Case Study 2: effect of drug concentration on U937 cell population

Case Study 2 investigates the effects of different concentrations of the topoisomerase II poison etoposide on the myeloid leukemia cells U937. Indeed, after exposure to low doses of etoposide, U937 undergo dramatic

morphological and functional changes [52], that potentially result in cell dielectric alterations. To this aim, a total number of 54 cells were measured, in particular, 22 untreated cells (3 replicas), 14 cells treated with 0.5 μM of etoposide for 1hr (3 replicas) and 15 cells treated with 1.0 μM of etoposide for 1hr (3 replicas). Treated cells and untreated ones exhibited both nDEP and pDEP at certain frequencies.

2.8.3 Case Study 3: effect of drug exposure time on PC3 cell population

Case Study 3 takes into account three experimental conditions for PC3 cells, untreated and treated with etoposide at two different exposure times (i.e., 3, 6 or 24 hours). PC3 cancer cells are derived from a castration-resistant, metastatic prostate cancer, displaying neuroendocrine features [53]; in such instances, patients are often treated with chemotherapy, including etoposide. We, therefore, use the clinically-relevant PC3/etoposide system to investigate the impact of different drug exposure times on the OET cell spectrum. As PC3 cells are less sensitive to etoposide-induced apoptosis than U937, we were able to increase the exposure time of the cells to the drug. A total number of 110 PC3 cells were measured, in particular 33 untreated cells (3 replicas), 30 cells treated with 0.5 μM of etoposide for 3hrs (1 replica), 21 cells treated with 0.5 μM of etoposide for 6hrs (1 replica), 26 cells treated with 0.5 μM of etoposide for 24hrs (1 replica). Treated cells exhibited only a pDEP force throughout the measurements.

3. Results and Discussions

The first analysis performed with the OET system consisted in verifying the system capability for particle handling. In particular, we investigated whether the main developments of the system setup and lab-on-chip device reported in this work, have improved the performance relative to standard OET. In particular, we investigated both the effects of the medium conductivity and the light pattern size on velocity and DEP force exerted on polystyrene particles. The obtained results were consistent with the literature. In fact, as expected and similarly to results reported by Witte et. al. (2020), we have found that both parameters increase with the increase of pattern size and decrease with the increase of medium conductivity. The details of this evaluation are reported in Supplementary materials. The capability of the proposed OET system in discriminating cells in different biological scenarios is evaluated with respect to the classification performance relative to the three case studies described in *Section 2.8*. For each scenario, a specific LDA model has been trained with the features automatically selected from the response spectra. The selected features, for each case study, are reported in Table S2.

3.1 Evaluation of OET system ability for cell manipulation

3.1.1 Case Study 1: discrimination of heterogeneous cell populations

In Case Study 1, we tested the ability of the OET system to distinguish diverse cell populations. Fig. 4(a) shows the response spectra obtained for $CD(f_n)$, (left panel), $v_{max}(f_n)$, (central panel), and $F_{DEP\_max}(f_n)$ (right panel). The frequency at which the response spectra of $CD(f_n)$ reach their maximum values corresponds to the crossover frequency, f_{co}, in light of the fact that a change of the sign of the DEP force, from nDEP to pDEP, corresponds to a decrease in the $CD(f_n)$ values, in accordance with Eq. 6. For the case of the response spectra of $v_{max}(f_n)$, instead, the f_{co}corresponds to the minimum as at that particular frequency cells change the motion direction. The same holds for the response spectra of $F_{DEP\_max}(f_n)$ according to Equations 11 and 12.

The response spectra of $CD(f_n)$ exhibit lower standard deviation values as compared to $v_{max}(f_n)$ and $F_{DEP\_max}(f_n)$ spectra. Left panel of Fig. 4(a) shows increasing values of the $CD(f_n)$ until the peak (nDEP force) and decreasing values after the f_{co} (pDEP force) for both U937 (in blue) and PC3 (in red) cells. Instead, HaCaT response spectrum (in green) presents only negative values and no peak is present along the curve, so cells exhibited only a pDEP force in the considered frequency range.

Similar considerations can be derived by considering the mean values of $v_{max}(f_n)$ and $F_{DEP\_max}(f_n)$ (shown in central and right panels of Fig. 4(a), respectively). The f_{co} corresponds to the minimum of the curves for U937 and PC3, whilst no minimum value is present in the spectrum response relative to HaCaT cells.

In particular, U937 and PC3 have, respectively, a f_{co} at around 40 kHz and 30 kHz (which is indicated in Fig. 4(a) by the blue and red dotted lines, respectively).
Table S3 reports the values of f_{co} , C_{mem}, and r. PC3 and HaCaT cells have similar r values, while U937 have a smaller size. However, due to the great quantity of information encoded within all of the three spectra for each cell type, we extrapolated this content of information to well distinguish the behaviour of U937, PC3 and HaCaT. A total number of two features was automatically selected to build the LDA model that reached an accuracy of 99.05% (2.13%) with all U937 and HaCaT cells correctly classified, on average, as shown in the confusion matrix of Fig. 5(a) (in the left panel). The score plot on canonical variables 1 and 2 is reported in the right panel of Fig.5(a). Indeed, two features are enough to extract the biologically carried information of the case study, in particular: $F_{DEP\_max}(f_{75kHz})$ and $F_{DEP\_max}(f_{80kHz})$ (see Table S2).
The observed differences in the dielectric behaviour of the three cell populations reflect their heterogeneity. In particular, U937 are cells cultured in suspension (i.e., they are in their standard biological condition during the OET analysis), whilst both PC3 and HaCaT are adherent cells that therefore needed to be trypsinized before the analysis. Unlike U937 and PC3, which are cancer cell lines, HaCaT are immortalized keratinocytes. Such different biological specifications are reflected by differences in f_{co} and C_{mem} values, as reported in Table S3 and also in the studies of Vaillier et al. [54].
It is important to stress that the ability of the proposed OET system to discriminate with high accuracy epithelial tumor cells from monocytes (i.e., no PC3 cell was misrecognized as U937 and vice versa) by combining specific physical descriptors, paves the way for its possible use as a novel tool to separate and analyse CTCs from patient-derived blood samples (i.e., liquid biopsies). Indeed, the isolation and characterization of CTCs from human blood is still a big clinical issue, far from being a routine procedure, due to technical problem of low abundance and uncertainties on the choice of the correct molecular determinants.

3.1.2 Case Study 2: effect of drug concentration on U937 cell population

Here, we evaluated the effect of different etoposide concentrations on U937cells. Fig. 4(b) shows the response spectra of untreated (corresponding to case study 1) and treated cells. In detail, U937 treated with 0.5 µM and 1 µM of etoposide show f_{co} = 55 kHz (indicated with the red dotted line) and f_{co} = 80 kHz (indicated with the green dotted line), respectively. Overall, an increase in drug concentration brought to a shift of f_{co} toward higher frequency values and, consequently, to a decrease of C_{mem} value. Such shift is in line with what is described by other authors in the literature by considering DEP-based systems [7,29]. In particular, Pethig et al. [33] reported the same trend for Jurkat T-cells (immortalized T lymphocytes), whilst Wang et al. [55] also observed the shift for HL-60 cells (human leukemia cell line). In our experiments, the medium conductivity is the same for all experiments and the cell radius does not significantly change during treatment, so, in accordance to Equation 5, the dependence of crossover frequency is only from membrane-specific capacitance. The latter is closely linked with the membrane composition and morphology such as microvilli, folds, ruffles etc. Thus, the shift in f_{co} occurring in treated U937 suggests an etoposide-induced membrane morphological/molecular modification related to the different drug concentrations [33,54,55]. Moreover, in etoposide-treated U937 an increase in cell size is revealed with respect to the untreated ones, as summarized in Table S3.
This information content was exploited by the combination of four selected features from the response spectra: $CD(f_{65kHz})$, $v_{max}(f_{95kHz})$, $F_{DEP\_max}(f_{70kHz})$ and $F_{DEP\_max}(f_{75kHz})$ (as reported in Table S2). Such features were used to build the classification model and the obtained results are reported in the confusion matrix of Fig. 5(b) (in the left panel). The model reaches an accuracy of 96.11% (5.41%), with all the cells treated at 1.0µM correctly recognized. The scores plot of the canonical variables 1 and 2 are illustrated in Fig. 5(b) (right panel).

3.1.3 Case Study 3: effect of drug exposure time on PC3 cell population

With Case Study 3, we investigated the effects of diverse etoposide exposure times on PC3 cancer cells.
Fig. 5(c) shows the response spectra with average of the three parameters for untreated (corresponding to the PC3 control for Case Study 1) and treated PC3. The latter does not present a f_{co} in the frequency range of [25-150] kHz but exhibits only a pDEP force, as indicted by the absence of a maximum point in the CD spectra and of minimum point in the maximum velocity and maximum DEP force spectra, respectively. Frequency

values in the range 25-50 kHz lead to death of treated PC3 cells. This may suggest a change in membrane dielectric characteristics induced by etoposide on PC3 [34].
In this case, the selected features are listed in Table S2. It is interesting to observe the arrangement of the scores on canonical variables 1 and 2 (Fig. 5(c) right panel). The canonical variable 1 provides discriminative information on the presence/absence of the drug (similarly to the Case Study 1) and the canonical variable 2 on the exposure time.
The classification results are reported in the confusion matrix of Fig. 5(c). In this case, we cross-validated the classification model on four classes: untreated, treated at 0.5 μM for 3 hrs, treated at 0.5 μM for 6 hrs and at 0.5 μM for 24 hrs. The accuracy reached was 89.32% with over the 90% of untreated cells and treated cells at 0.5 μM for 3 hrs and 6hrs are correctly recognized, instead some treated cells at 0.5 μM for 24hrs were misrecognized as treated at 0.5 μM for 6hrs. The obtained results suggest the capability of the system to differentiate cell populations either based on physicochemical properties like size and shape, or electric properties, like conductivity/permittivity and membrane capacitance.
To determine the limits of the proposed system, we also reported an example of cell behaviour under a high etoposide concentration of 5.0 μM for 24hrs. In Figure 6, the descriptors obtained with 16 cells under treatments of 0.5 μM for 24 hrs are compared with those obtained at a concentration of 5.0 μM for 24 hrs. $CD(f_n)$ is unable to separate the two cell populations (left panel), whilst $v_{max}(f_n)$ and $F_{DEP\_max}(f_n)$ spectra exhibit a saturation behaviour, as shown in the central and right panels of Fig 6, respectively. This is due to stronger DEP force values produced with respect to the other case scenarios, which limit the dynamics of the observed responses. Therefore, the discrimination of the drug concentrations with an exposure time equal or higher than 6 hrs would require a greater distance between the starting point of the cell and the centre of the rectangular light pattern.

3.2 Evaluation of standard dielectric parameters ability in cell discrimination

Although crossover frequency or membrane capacitance have proved to be useful to understand cell behaviour [19,32,34,54], the heterogeneity of cell characteristics and responses to diversified external stimuli, requires more in depth analyses. In particular, we have shown how the combination of diverse features carefully selected over multi-frequency spectra can reflect the cell's photo-induced motion.
To prove this aspect, a further analysis was performed for the Case Study 2, which is the only one in which the f_{co} was present for all of the discriminative categories in the analysed frequency range. We compared the obtained results with those achieved by an LDA classification model built considering three static features: cells radius, crossover frequency and membrane capacitance (we called it *standard method* to refer to the standard dielectric parameters used). The obtained classification results are reported in the confusion matrix in Fig. S7(a). The model reaches an accuracy of 69%, and fails in recognizing the cells treated with 0.5 μM of etoposide drug. The proposed method instead, being based on the features extracted from the response spectra, reaches an accuracy of 96% (as shown in Fig. S7(b)). Therefore, the information content in spectra parameters, for a certain frequency range, is able to distinguish diverse cell populations in different case studies without necessarily knowing the f_{co} values, like in Case Study 1 and 3.
The obtained results support the idea that the information content to be extracted via OET-based devices in order to recognize univocally a biological scenario may not be conveyed by static parameters like cells radius, f_{co}, and C_{mem}. On the contrary, response spectra derived via multiple frequency observations were capable of providing effective characterizations of the cell dielectric properties. The proposed OET configuration, limited the stress induced on the cells during the measurement and facilitated longer observation times in multi-frequency steps. The optimal set of features and corresponding frequencies of interest have been defined for each biological scenario as OET cell signature. Once the model is defined, subsequent studies on the same experiment can be performed without the need of analysing the complete range of frequencies but using the selected features only, so that the measuring time and cellular stress can be furtherly reduced.
It is important to stress that, in an unprecedented way with respect to the classical cytometry, the proposed platform allows to extract a deeper inside of cell properties and reactions to external stimuli such as drugs, able to recognize the dose level in terms of individual frequency spectra content. With the support of a machine learning processing strategy (in this work sequential forward feature selection and classification model), the

information content blinded inside the frequency spectra may be fully exploited and adapted to the specific case study. Even if the analysis of a multitude of data may require increased computation time, the platform is flexible to parallelization thanks to multi-positioning facilities and putting cells in different fields of view. It is expected that different frequency ranges may reveal a connection with further cell events, like apoptosis or necrosis phenomena, or highlight differences due to some genotype modifications that are not straightforward optically observed.

4. Conclusions

The early detection and the accurate discrimination of different biological events through dielectric responses of single cells can be a useful support to cancer diagnosis and prognosis, and to study the therapeutic potential of novel compounds. To achieve this goal, we designed and realized a novel integrated OET system, which is able to cut down the power transmitted on the LOC device, therefore reducing evaporation and warming of the culture media during the experiments, therefore increasing the viability of the observed cells.
A novel point of view was then addressed to better understand the information content encoded in the dielectric responses for diverse biological scenarios. What has emerged is that a single dielectric parameter provides a general overview of the cell characteristics, intrinsic or in response to an external stimulus, such as a chemotherapy insult, but a deeper and multi-frequency analysis is needed to accurately distinguish different cell populations and biological phenomena. Future studies handling the analysis in parallel of cells to speed up the overall procedure and derive multiple measurements at a time, will open the window to invaluable applicative potentials of OET in the clinic.

References

[1] A. De Ninno, R. Reale, A. Giovinazzo, F.R. Bertani, L. Businaro, P. Bisegna, C. Matteucci, F. Caselli, High-throughput label-free characterization of viable, necrotic and apoptotic human lymphoma cells in a coplanar-electrode microfluidic impedance chip, Biosens. Bioelectron. 150 (2020) 111887. https://doi.org/10.1016/j.bios.2019.111887.

[2] F. Alnaimat, S. Dagher, B. Mathew, A. Hilal-Alnqbi, S. Khashan, Microfluidics Based Magnetophoresis: A Review, Chem. Rec. 18 (2018) 1596–1612. https://doi.org/10.1002/tcr.201800018.

[3] X. Chen, Z. Liang, D. Li, Y. Xiong, P. Xiong, Y. Guan, S. Hou, Y. Hu, S. Chen, G. Liu, Y. Tian, Microfluidic dielectrophoresis device for trapping, counting and detecting Shewanella oneidensis at the cell level, Biosens. Bioelectron. 99 (2018) 416–423. https://doi.org/10.1016/j.bios.2017.08.017.

[4] Y. Zhang, J. Zhao, H. Yu, P. Li, W. Liang, Z. Liu, G.B. Lee, L. Liu, W.J. Li, Z. Wang, Detection and isolation of free cancer cells from ascites and peritoneal lavages using optically induced electrokinetics (OEK) (Science Advances DOI: 10.1126/sciadv.aba9628), Sci. Adv. 6 (2020) 1–14. https://doi.org/10.1126/sciadv.abf1937.

[5] S. Kar, P. Shinde, M. Nagai, T.S. Santra, Optical Manipulation of Cells, in: Microfluid. Bio-MEMS, 2020: pp. 49–94. https://doi.org/10.1201/9781003014935-2.

[6] J.K. Valley, A. Jamshidi, A.T. Ohta, H.Y. Hsu, M.C. Wu, Operational regimes and physics present in optoelectronic tweezers, J. Microelectromechanical Syst. 17 (2008) 342–350. https://doi.org/10.1109/JMEMS.2008.916335.

[7] W.P. Chou, H.M. Wang, J.H. Chang, T.K. Chiu, C.H. Hsieh, C.J. Liao, M.H. Wu, The utilization of optically-induced-dielectrophoresis (ODEP)-based virtual cell filters in a microfluidic system for continuous isolation and purification of circulating tumour cells (CTCs) based on their size characteristics, Sens. Actuators B Chem. 241 (2017) 245–254. https://doi.org/10.1016/j.snb.2016.10.075.

[8] T.K. Chiu, A.C. Chao, W.P. Chou, C.J. Liao, H.M. Wang, J.H. Chang, P.H. Chen, M.H. Wu, Optically-induced-dielectrophoresis (ODEP)-based cell manipulation in a microfluidic system for high-purity isolation of integral circulating tumor cell (CTC) clusters based on their size characteristics, Sens. Actuators B Chem. 258 (2018) 1161–1173. https://doi.org/10.1016/j.snb.2017.12.003.

[9] S. Bin Huang, M.H. Wu, Y.H. Lin, C.H. Hsieh, C.L. Yang, H.C. Lin, C.P. Tseng, G. Bin Lee, High-purity and label-free isolation of circulating tumor cells (CTCs) in a microfluidic platform by using optically-induced-dielectrophoretic (ODEP) force, Lab Chip. 13 (2013) 1371–1383. https://doi.org/10.1039/c3lc41256c.

[10] S. Bin Huang, S.L. Liu, J.T. Li, M.H. Wu, Label-free live and dead cell separation method using a high-efficiency optically-induced dielectrophoretic (ODEP) force-based microfluidic platform, Int. J. Autom. Smart Technol. 4 (2014) 83–91. https://doi.org/10.5875/ausmt.v4i2.302.

[11] P.Y. Chiou, A.T. Ohta, A. Jamshidi, H.Y. Hsu, M.C. Wu, Light-actuated AC electroosmosis for nanoparticle manipulation, J. Microelectromechanical Syst. 17 (2008) 525–531. https://doi.org/10.1109/JMEMS.2008.916342.

[12] H. Hwang, J.K. Park, Rapid and selective concentration of microparticles in an optoelectrofluidic platform, Lab Chip. 9 (2009) 199–206. https://doi.org/10.1039/b811740c.

[13] N.G. Green, A. Ramost, A. González, A. Castellanos, H. Morgan, Electric field induced fluid flow on microelectrodes: The effect of illumination, J. Phys. D. Appl. Phys. 33 (2000). https://doi.org/10.1088/0022-3727/33/2/102.

[14] P.Y. Chiou, A.T. Ohta, M.C. Wu, Massively parallel manipulation of single cells and microparticles using optical images, Nature. 436 (2005) 370–372. https://doi.org/10.1038/nature03831.

[15] K.-W. Huang, Y.-C. Wu, J.-A. Lee, P.-Y. Chiou, Microfluidic Integrated Optoelectronic Tweezers for Single-cell Preparation and Analysis, Lab Chip. 13 (2013) 3721–3727.

[16] Y.H. Lin, G. Bin Lee, Optically induced flow cytometry for continuous microparticle counting and sorting, Biosens. Bioelectron. 24 (2008) 572–578. https://doi.org/10.1016/j.bios.2008.06.008.

[17] S. Zhang, J. Juvert, J.M. Cooper, S.L. Neale, Manipulating and assembling metallic beads with Optoelectronic Tweezers, Sci. Rep. 6 (2016) 1–10. https://doi.org/10.1038/srep32840.

[18] C. Witte, J. Reboud, J.M. Cooper, S.L. Neale, Channel integrated optoelectronic tweezer chip for microfluidic particle manipulation, J. Micromechanics Microengineering. 30 (2020). https://doi.org/10.1088/1361-6439/ab6c72.

[19] N. Liu, Y. Lin, Y. Peng, L. Xin, T. Yue, Y. Liu, C. Ru, S. Xie, L. Dong, H. Pu, H. Chen, W.J. Li, Y. Sun, Automated Parallel Electrical Characterization of Cells Using Optically-Induced Dielectrophoresis, IEEE Trans. Autom. Sci. Eng. 17 (2020) 1084–1092. https://doi.org/10.1109/TASE.2019.2963044.

[20] K.W. Huang, T.W. Su, A. Ozcan, P.Y. Chiou, Optoelectronic tweezers integrated with lensfree holographic microscopy for wide-field interactive cell and particle manipulation on a chip, Lab Chip. 13 (2013) 2278–2284. https://doi.org/10.1039/c3lc50168j.

[21] S.L. Neale, A.T. Ohta, H.-Y. Hsu, J.K. Valley, A. Jamshidi, M.C. Wu, Trap profiles of projector based optoelectronic tweezers (OET) with HeLa cells, Opt. Express. 17 (2009) 5231. https://doi.org/10.1364/oe.17.005231.

[22] A.T. Ohta, P.Y. Chiou, H.L. Phan, S.W. Sherwood, J.M. Yang, A.N.K. Lau, H.Y. Hsu, A. Jamshidi, M.C. Wu, Optically controlled cell discrimination and trapping using optoelectronic tweezers, IEEE J. Sel. Top. Quantum Electron. 13 (2007) 235–242. https://doi.org/10.1109/JSTQE.2007.893558.

[23] T.K. Chiu, W.P. Chou, S. Bin Huang, H.M. Wang, Y.C. Lin, C.H. Hsieh, M.H. Wu, Application of optically-induced-dielectrophoresis in microfluidic system for purification of circulating tumour cells for gene expression analysis-Cancer cell line model, Sci. Rep. 6 (2016) 1–14. https://doi.org/10.1038/srep32851.

[24] P.Y. Chu, C.J. Liao, C.H. Hsieh, H.M. Wang, W.P. Chou, P.H. Chen, M.H. Wu, Utilization of optically induced dielectrophoresis in a microfluidic system for sorting and isolation of cells with varied degree of viability: Demonstration of the sorting and isolation of drug-treated cancer cells with various degrees of anti-cancer dru, Sens. Actuators B Chem. 283 (2019) 621–631. https://doi.org/10.1016/j.snb.2018.12.047.

[25] C. Gabriel, Dielectric properties of biological materials, in: Bioeng. Biophys. Asp. Electromagn. Fields, Press, New York: CRC, 2006: pp. 52–81.

[26] W. Liang, Y. Zhao, L. Liu, Y. Wang, W.J. Li, G. Bin Lee, Determination of Cell Membrane Capacitance and Conductance via Optically Induced Electrokinetics, Biophys. J. 113 (2017) 1531–1539. https://doi.org/10.1016/j.bpj.2017.08.006.

[27] W. Liang, K. Zhang, X. Yang, L. Liu, H. Yu, W. Zhang, Distinctive translational and self-rotational motion of lymphoma cells in an optically induced non-rotational alternating current electric field, Biomicrofluidics. 9 (2015) 1–16. https://doi.org/10.1063/1.4913365.

[28] F.H. Labeed, H.M. Coley, M.P. Hughes, Differences in the biophysical properties of membrane and cytoplasm of apoptotic cells revealed using dielectrophoresis, Biochim. Biophys. Acta - Gen. Subj. 1760 (2006) 922–929. https://doi.org/10.1016/j.bbagen.2006.01.018.

[29] A.T. Ohta, P.-Y. Chiou, A. Jamshidi, H.-Y. Hsu, J.K. Valley, S.L. Neale, M.C. Wu, Optoelectronic Tweezers for the Manipulation of Cells, Microparticles, and Nanoparticles, Recent Opt. Photonic Technol. (2010). https://doi.org/10.5772/6921.

[30] S. Zhang, N. Shakiba, Y. Chen, Y. Zhang, P. Tian, J. Singh, M.D. Chamberlain, M. Satkauskas, A.G. Flood, N.P. Kherani, S. Yu, P.W. Zandstra, A.R. Wheeler, Patterned Optoelectronic Tweezers: A New Scheme for Selecting, Moving, and Storing Dielectric Particles and Cells, Small. 14 (2018) 1–11. https://doi.org/10.1002/smll.201803342.

[31] T.B. Jones, Electromechanics of particles, Cambridge university press, 2005.

[32] N. Nasir, M. Al Ahmad, Cells Electrical Characterization: Dielectric Properties, Mixture, and Modeling Theories, J. Eng. (United Kingdom). 2020 (2020). https://doi.org/10.1155/2020/9475490.

[33] R. Pethig, M.S. Talary, Dielectrophoretic detection of membrane morphology changes in Jurkat T-cells undergoing etoposide-induced apoptosis, IET Nanobiotechnology. 1 (2007) 2–9. https://doi.org/10.1049/iet-nbt:20060018.

[34] I. Turcan, M.A. Olariu, Dielectrophoretic Manipulation of Cancer Cells and Their Electrical Characterization, ACS Comb. Sci. 22 (2020) 554–578. https://doi.org/10.1021/acscombsci.0c00109.

[35] H.Y. Hsu, A.T. Ohta, P.Y. Chiou, A. Jamshidi, S.L. Neale, M.C. Wu, Phototransistor-based optoelectronic tweezers for dynamic cell manipulation in cell culture media, Lab Chip. 10 (2010) 165–172.

https://doi.org/10.1039/b906593h.

[36] Y.K. Hwang, N. Ahuja, A Potential Field Approach to Path Planning, IEEE Trans. Robot. Autom. 8 (1992) 23–32. https://doi.org/10.1109/70.127236.

[37] F.G. Ding, P. Jiao, X.Q. Bian, H.J. Wang, AUV local path planning based on virtual potential field, IEEE Int. Conf. Mechatronics Autom. ICMA 2005. (2005) 1711–1716. https://doi.org/10.1109/icma.2005.1626816.

[38] M. Nguyen, A. De Ninno, A. Mencattini, F. Mermet-Meillon, G. Fornabaio, S.S. Evans, M. Cossutta, Y. Khira, W. Han, P. Sirven, F. Pelon, D. Di Giuseppe, F.R. Bertani, A. Gerardino, A. Yamada, S. Descroix, V. Soumelis, F. Mechta-Grigoriou, G. Zalcman, J. Camonis, E. Martinelli, L. Businaro, M.C. Parrini, Dissecting Effects of Anti-cancer Drugs and Cancer-Associated Fibroblasts by On-Chip Reconstitution of Immunocompetent Tumor Microenvironments, Cell Rep. 25 (2018) 3884-3893.e3. https://doi.org/10.1016/j.celrep.2018.12.015.

[39] D. Di Giuseppe, F. Corsi, A. Mencattini, M.C. Comes, P. Casti, C. Di Natale, L. Ghibelli, E. Martinelli, Learning Cancer-Related Drug Efficacy Exploiting Consensus in Coordinated Motility within Cell Clusters, IEEE Trans. Biomed. Eng. 66 (2019) 2882–2888. https://doi.org/10.1109/TBME.2019.2897825.

[40] M. D'Orazio, F. Corsi, A. Mencattini, D. Di Giuseppe, M. Colomba Comes, P. Casti, J. Filippi, C. Di Natale, L. Ghibelli, E. Martinelli, Deciphering Cancer Cell Behavior From Motility and Shape Features: Peer Prediction and Dynamic Selection to Support Cancer Diagnosis and Therapy, Front. Oncol. 10 (2020) 1–11. https://doi.org/10.3389/fonc.2020.580698.

[41] M.C. Comes, J. Filippi, A. Mencattini, F. Corsi, P. Casti, A. De Ninno, D. Di Giuseppe, M. D'Orazio, L. Ghibelli, F. Mattei, G. Schiavoni, L. Businaro, C. Di Natale, E. Martinelli, Accelerating the experimental responses on cell behaviors: a long-term prediction of cell trajectories using Social Generative Adversarial Network, Sci. Rep. 10 (2020) 1–17. https://doi.org/10.1038/s41598-020-72605-3.

[42] M.C. Comes, P. Casti, A. Mencattini, D. Di Giuseppe, F. Mermet-Meillon, A. De Ninno, M.C. Parrini, L. Businaro, C. Di Natale, E. Martinelli, The influence of spatial and temporal resolutions on the analysis of cell-cell interaction: a systematic study for time-lapse microscopy applications, Sci. Rep. 9 (2019) 1–11. https://doi.org/10.1038/s41598-019-42475-5.

[43] E.R. Davies, Machine vision: theory, algorithms, practicalities, Elsevier, 2004.

[44] J. Munkres, Algorithms for the Assignment and Transportation Problems, J. Soc. Ind. Appl. Math. 5 (1957) 32–38.

[45] P.M. Anselone, P.J. Laurent, A general method for the construction of interpolating or smoothing spline-functions, Numer. Math. 12 (1968) 66–82. https://doi.org/10.1007/BF02170998.

[46] J. Leach, H. Mushfique, S. Keen, R. Di Leonardo, G. Ruocco, J.M. Cooper, M.J. Padgett, Comparison of Faxén's correction for a microsphere translating or rotating near a surface, Phys. Rev. E - Stat. Nonlinear, Soft Matter Phys. 79 (2009) 1–4. https://doi.org/10.1103/PhysRevE.79.026301.

[47] J. Happel, H. Brenner, Wall Effects on the Motion of a Single Particle, (1983) 286–357. https://doi.org/10.1007/978-94-009-8352-6_7.

[48] D.W. Aha, R.L. Bankert, A Comparative Evaluation of Sequential Feature Selection Algorithms, in: Lect. Notes Stat. – Proc., 2009: p. 341.

[49] G. Borboudakis, I. Tsamardinos, Forward-backward selection with early dropping, J. Mach. Learn. Res. 20 (2019) 1–39.

[50] M. Badiola-Mateos, D. Di Giuseppe, R. Paoli, M.J. Lopez-Martinez, A. Mencattini, J. Samitier, E. Martinelli, A novel multi-frequency trans-endothelial electrical resistance (MTEER) sensor array to monitor blood-brain barrier integrity, Sens. Actuators B Chem. 334 (2021) 129599. https://doi.org/10.1016/j.snb.2021.129599.

[51] D. Ballabio, V. Consonni, Classification tools in chemistry. Part 1: Linear models. PLS-DA, Anal. Methods. 5 (2013) 3790–3798. https://doi.org/10.1039/c3ay40582f.

[52] L. Ghibelli, Lowering Etoposide Doses Shifts Cell Demise From Caspase-Dependent to Differentiation and Caspase-3-Independent Apoptosis via DNA Damage Response , Inducing AML Culture Extinction, 9 (2018) 1–13. https://doi.org/10.3389/fphar.2018.01307.

[53] M.E. Kaighn, K.S. Narayan, Y. Ohnuki, J.F. Lechner, L.W. Jones, Establishment and characterization of a human prostatic carcinoma cell line (PC-3), Invest. Urol. 17 (1979) 16–23.

[54] C. Vaillier, T. Honegger, F. Kermarrec, X. Gidrol, D. Peyrade, Label-Free Electric Monitoring of Human Cancer Cells as a Potential Diagnostic Tool, Anal. Chem. 88 (2016) 9022–9028. https://doi.org/10.1021/acs.analchem.6b01648.

[55] X. Wang, F.F. Becker, P.R.C. Gascoyne, Membrane dielectric changes indicate induced apoptosis in HL-60 cells more sensitively than surface phosphatidylserine expression or DNA fragmentation, Biochim. Biophys. Acta - Biomembr. 1564 (2002) 412–420. https://doi.org/10.1016/S0005-2736(02)00495-9.

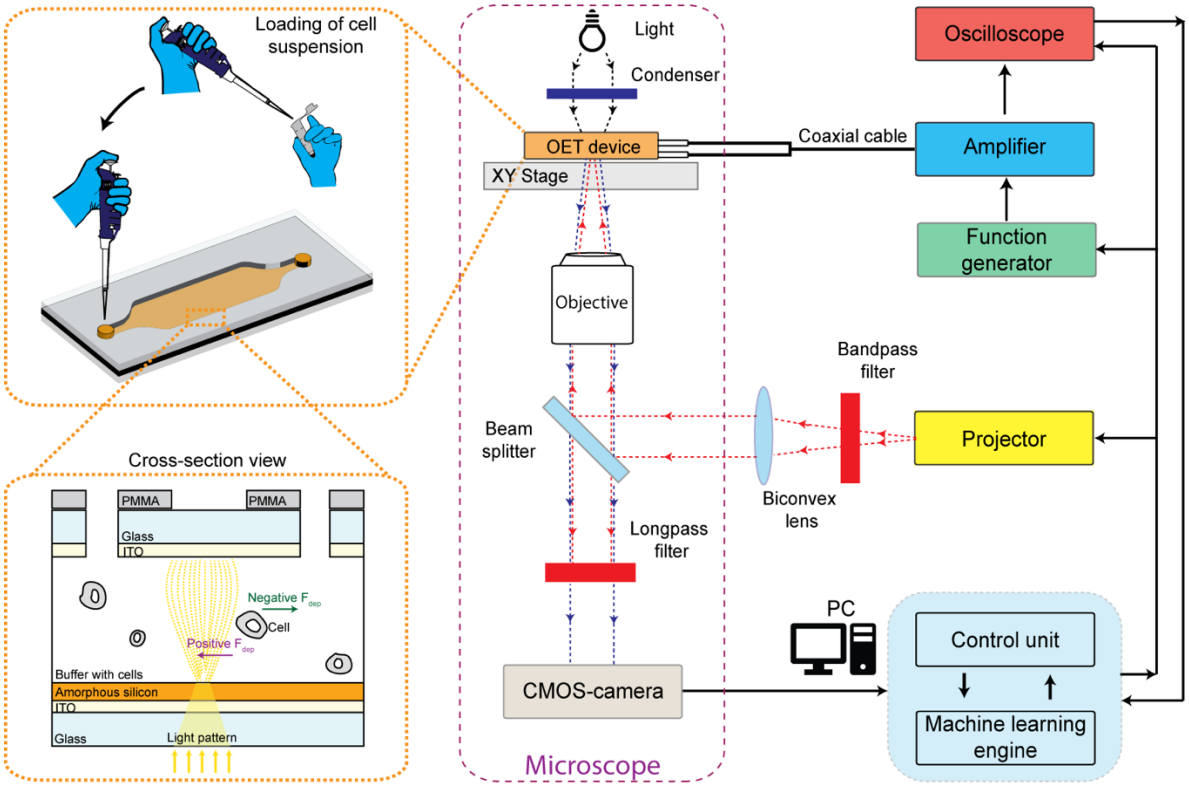

Fig. 1. Schematic illustration of the proposed integrated system for OET-based manipulation and characterization of cells. The system is composed of five main blocks: the microscope, the OET device in which cells are pipetted and manipulated, the AC voltage generator (composed of a function generator, an amplifier and an oscilloscope), a digital projector, and a PC station with a control unit and a machine learning engine.

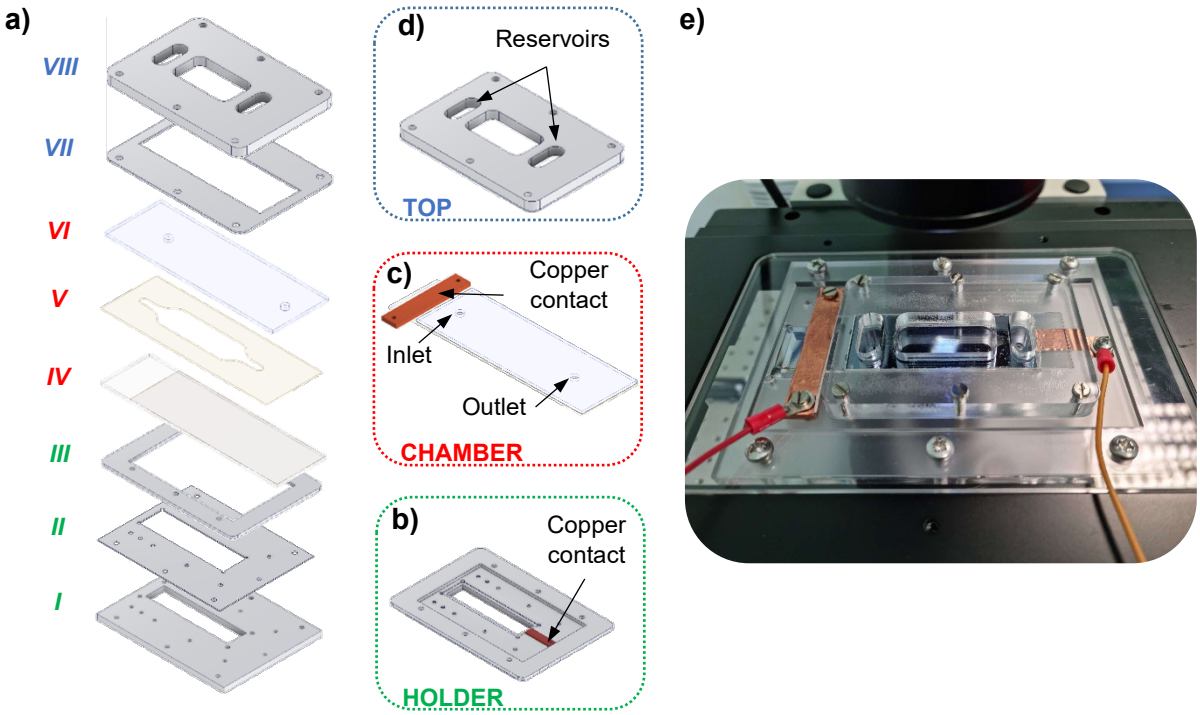

Fig. 2. (a) Exploded view of OET-based device: I, II base for bottom part of chip's chamber; III adapter for microscope's stage, IV ITO-coated glass and a-Si (bottom slide); V double side adhesive tape for chip channel; VI ITO-coated glass (top slide); VII base for top part of chip's chamber; VIII reservoirs. (b) Assembly of the holder part with the copper contact for the top slide, it comprises layers: I, II, III. (c) Assembly of the chamber part with the copper contact for the bottom slide. The top slide shows the inlet and outlet of the actual microfluidic part of the device. It comprises layers: IV, V, VI. (d) Assembly of top part. It comprises layers: VII and VIII. (e) Picture of the fabricated device.

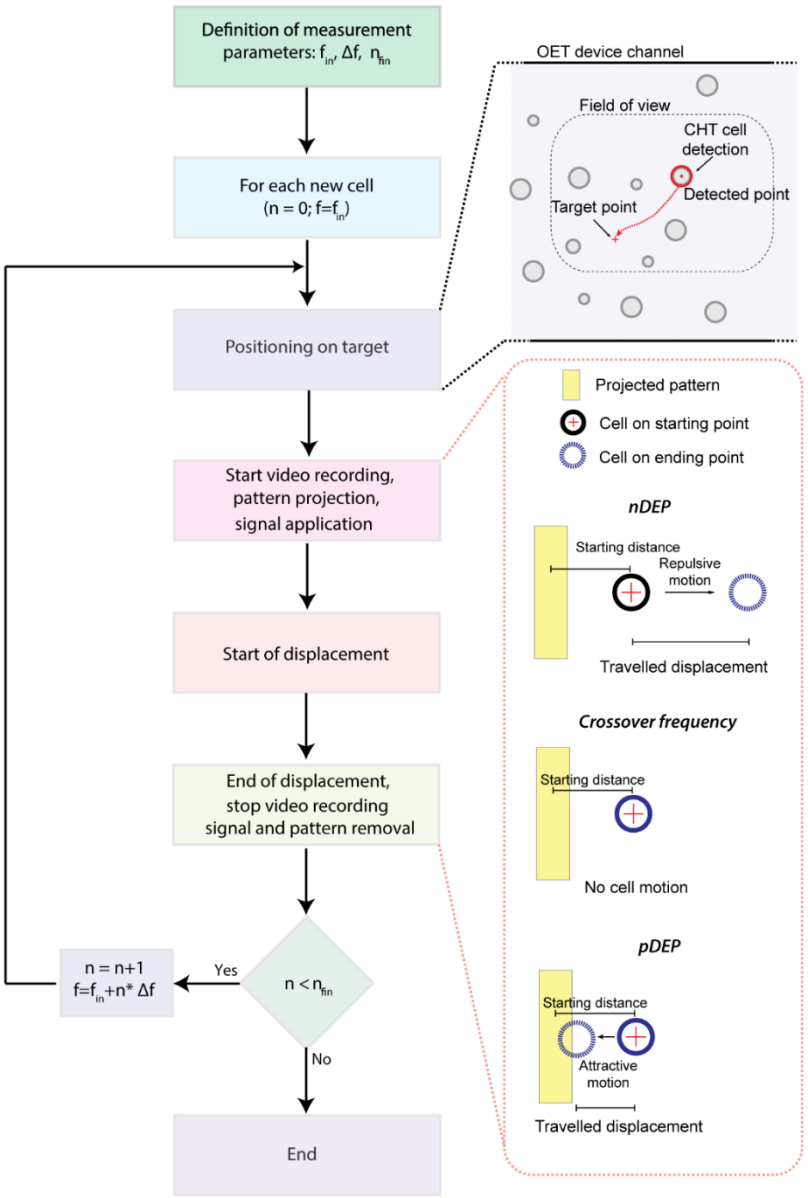

Fig. 3. Schematic representation of the OET-based experimental protocol. The dark zoom window represents the cell detection within a chosen field of view inside the chamber of the OET device and controlled motion toward the target point. The orange window reports the cell behaviour under a nDEP force, a crossover frequency, and a pDEP force during video recording.

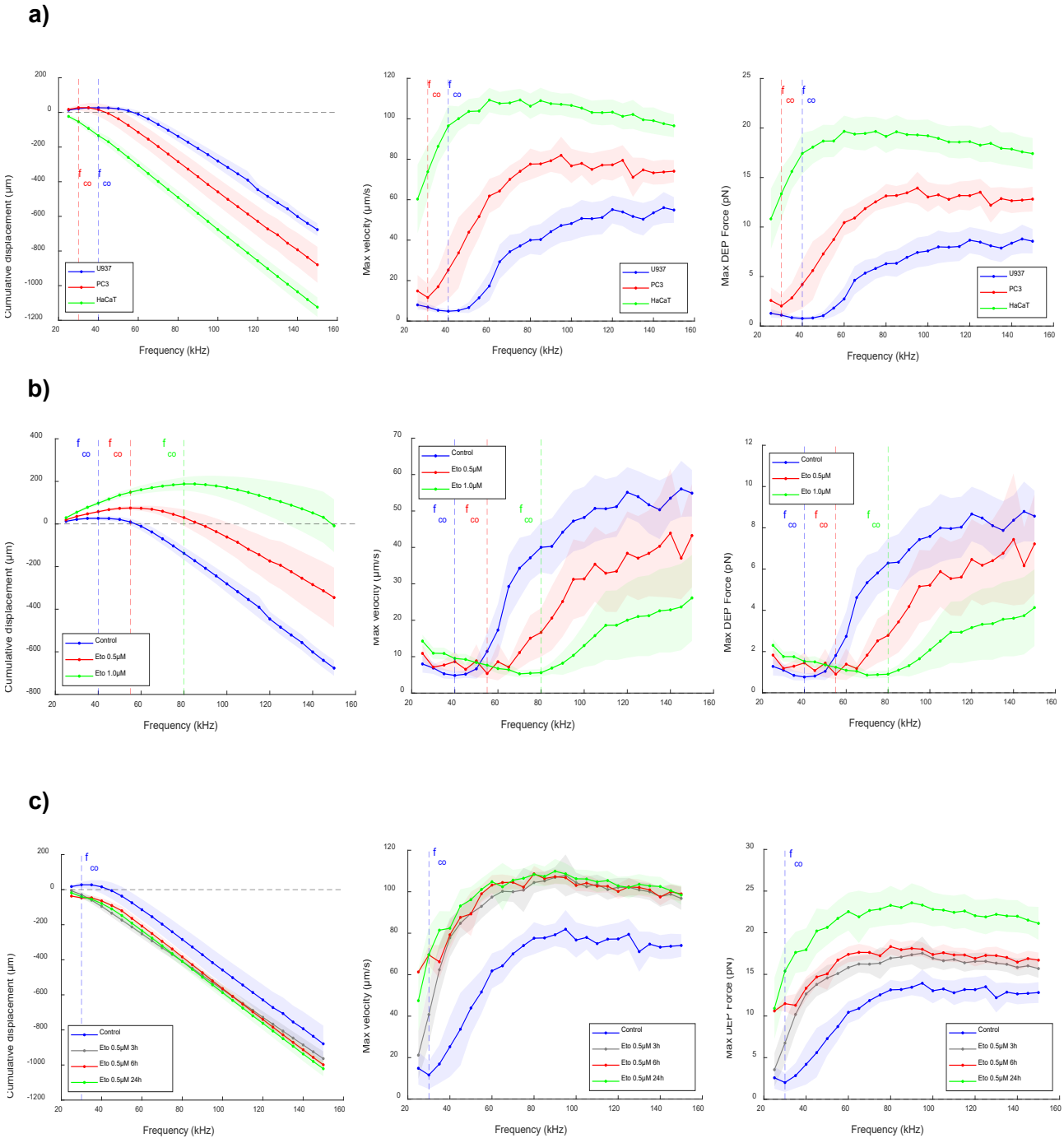

Fig. 4. Spectra of cumulative displacement (left panel), maximum velocity (central panel) and maximum DEP force (right panel) for case study 1 **(a)**, case study 2 **(b)** and case study 3 **(c)**. Average values are reported along the curves and the corresponding half standard deviation values are indicated with coloured shadows for better visualization. Dotted lines indicate the crossover frequency (f_{co}) values corresponding to the maximum values of the average cumulative displacement and to the minimum values of the average maximum velocity and maximum DEP force.

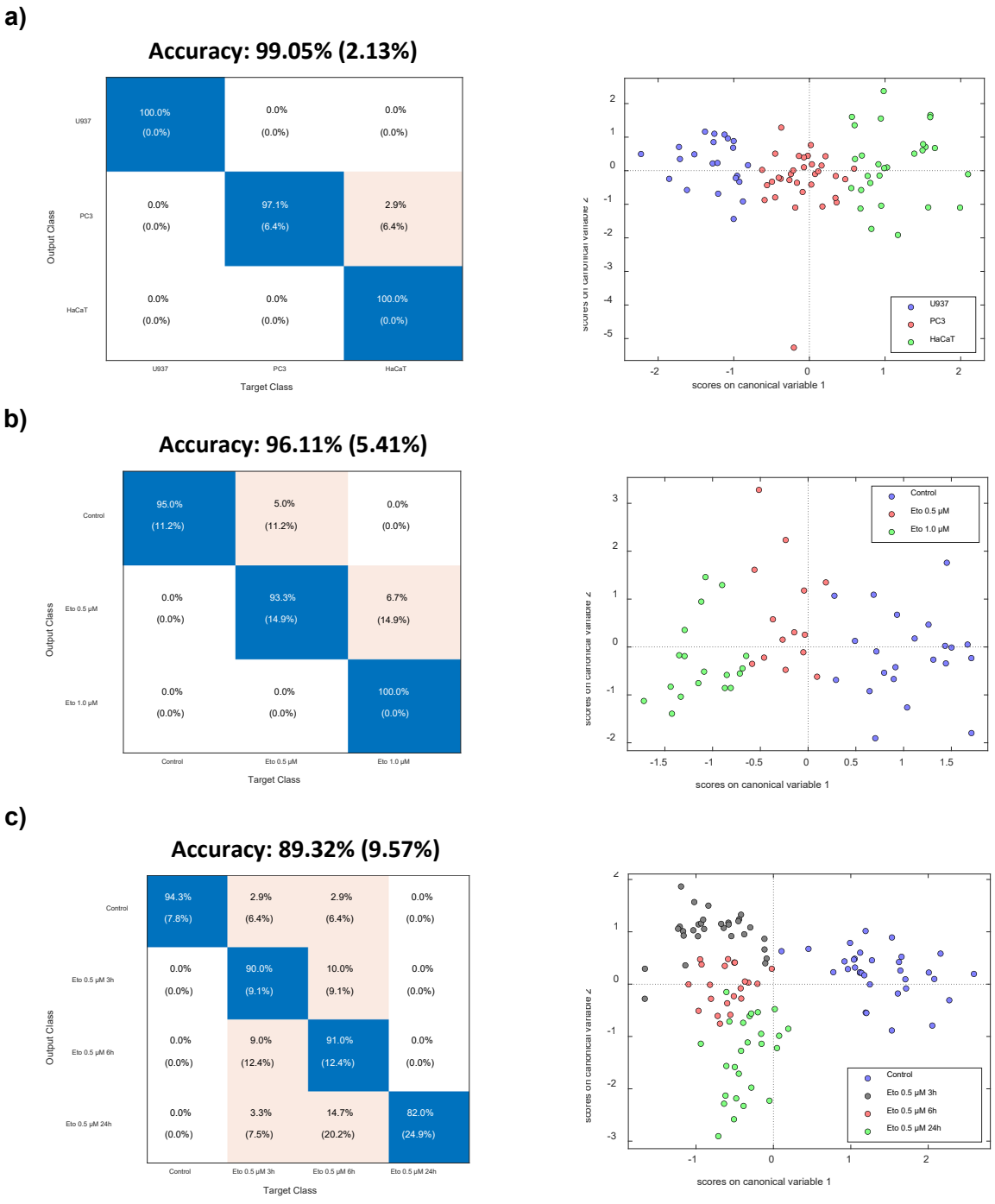

Fig. 5. Confusion matrix and accuracy value (left panel) and scores on canonical variable 1 and 2 (right panel) of the LDA classification model for Case Study 1 **(a)**, Case Study 2 **(b)** and Case Study 3 **(c).** The average (and standard deviation) values obtained over the rounds of venetian blind cross-validation are reported.

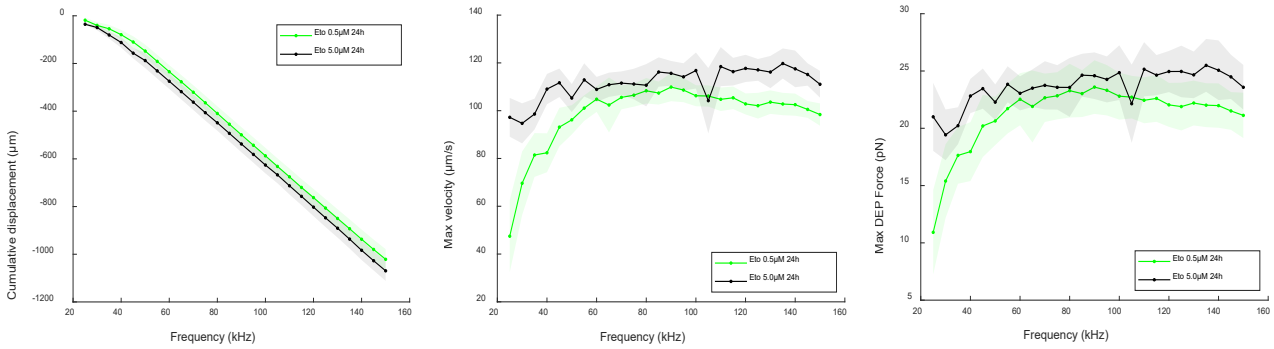

Fig. 6. Spectra of cumulative displacement (left panel), maximum velocity (central panel) and maximum DEP force (right panel) for Case Study 3. Average values are reported along the curves and the corresponding half standard deviation values are indicated with coloured shadows for better visualization.